ELECTRONIC SUPPLEMENTARY INFORMATION

Covalent Organic Frameworks-Based Li-S Batteries: Functional Separators Promoting Li^+ Transport and Polysulfide Trapping

Sara Gullace, Matteo Abruzzese, Luca Cusin, Gabriele Saleh, Sanjay B. Thorat, Agnese Gamberini, Sebastiano Bellani, Artur Ciesielski, Francesco Bonaccorso, Paolo Samorì*

Table S1. List of the COF-modified separators and their specifications (COF-based coating composition and areal weight) in comparison to bare Celgard2400 separator.

Separator	COF:SP:PVDF[a]	Areal weight (mg cm^{-2})
Pristine Celgard	-	1.35
K60@Celgard	60:30:10	1.65
KS60@Celgard (COF KS1)	60:30:10	1.75
KS80@Celgard (COF KS1)	80:10:10	1.66

[a] weight ratio in the COF-coating

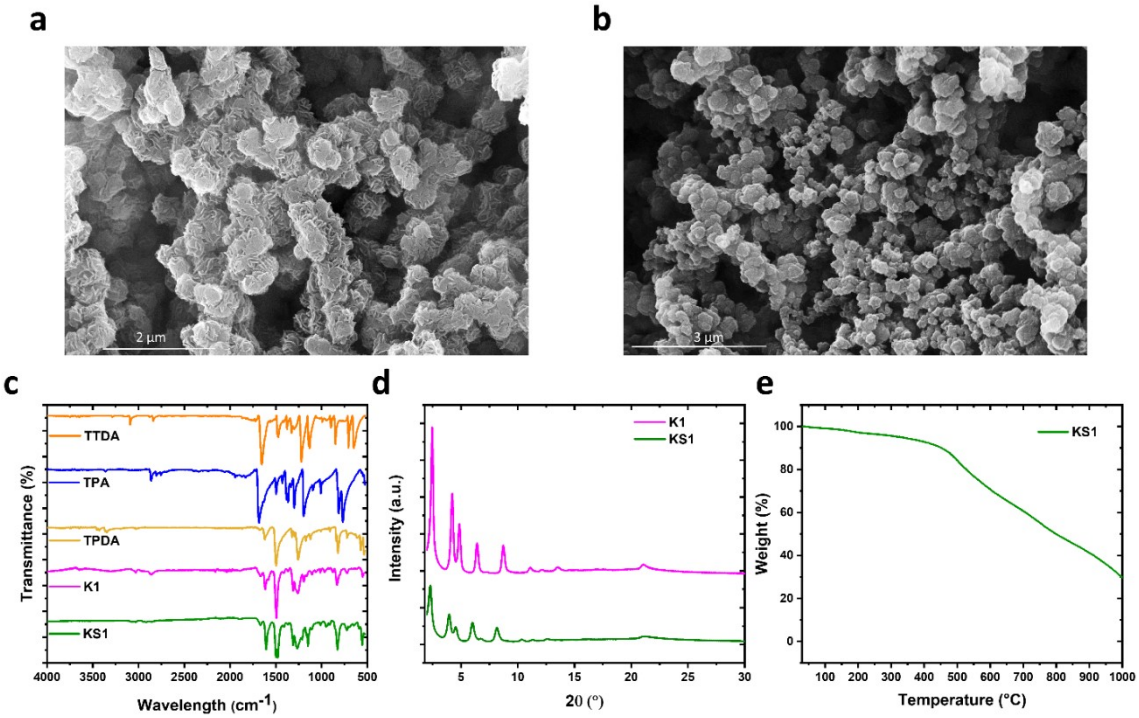

Figure S1. SEM images of the synthesized COFs (a) K1 and (b) KS1. (c) FT-IR spectra of the TPDA, TPA and TTDA monomers and the synthesized K1 and KS1 COFs. (d) PXRD patterns of K1 and KS1 COFs. (e) TGA profile of KS1 COF.

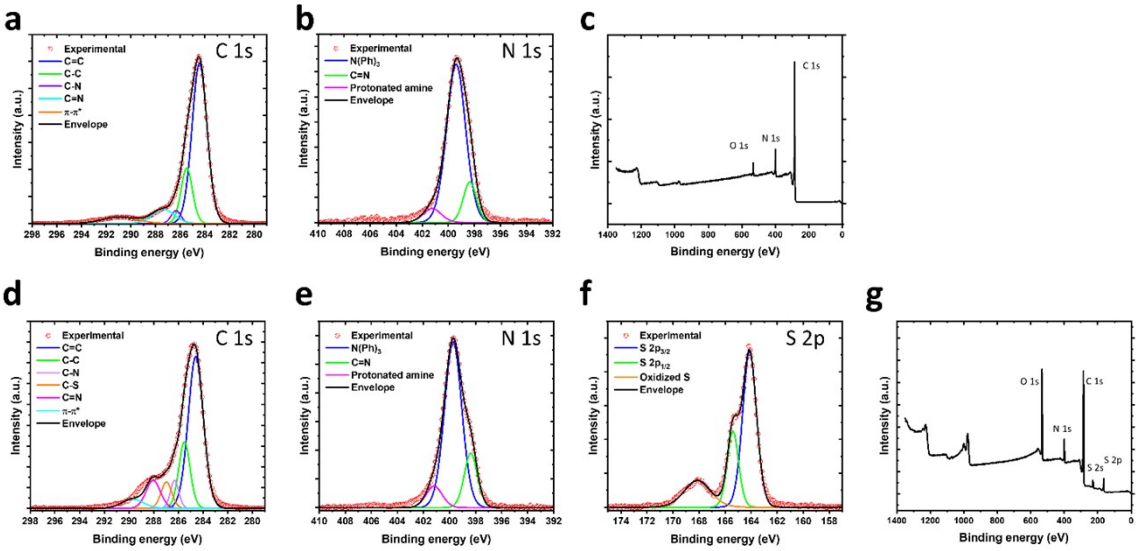

Figure S2. XPS spectra of (a-d) C 1s, (b-e) N 1s, (f) S 2p and (c-g) survey for (a-c) COF K1 and (d-g) COF KS1.

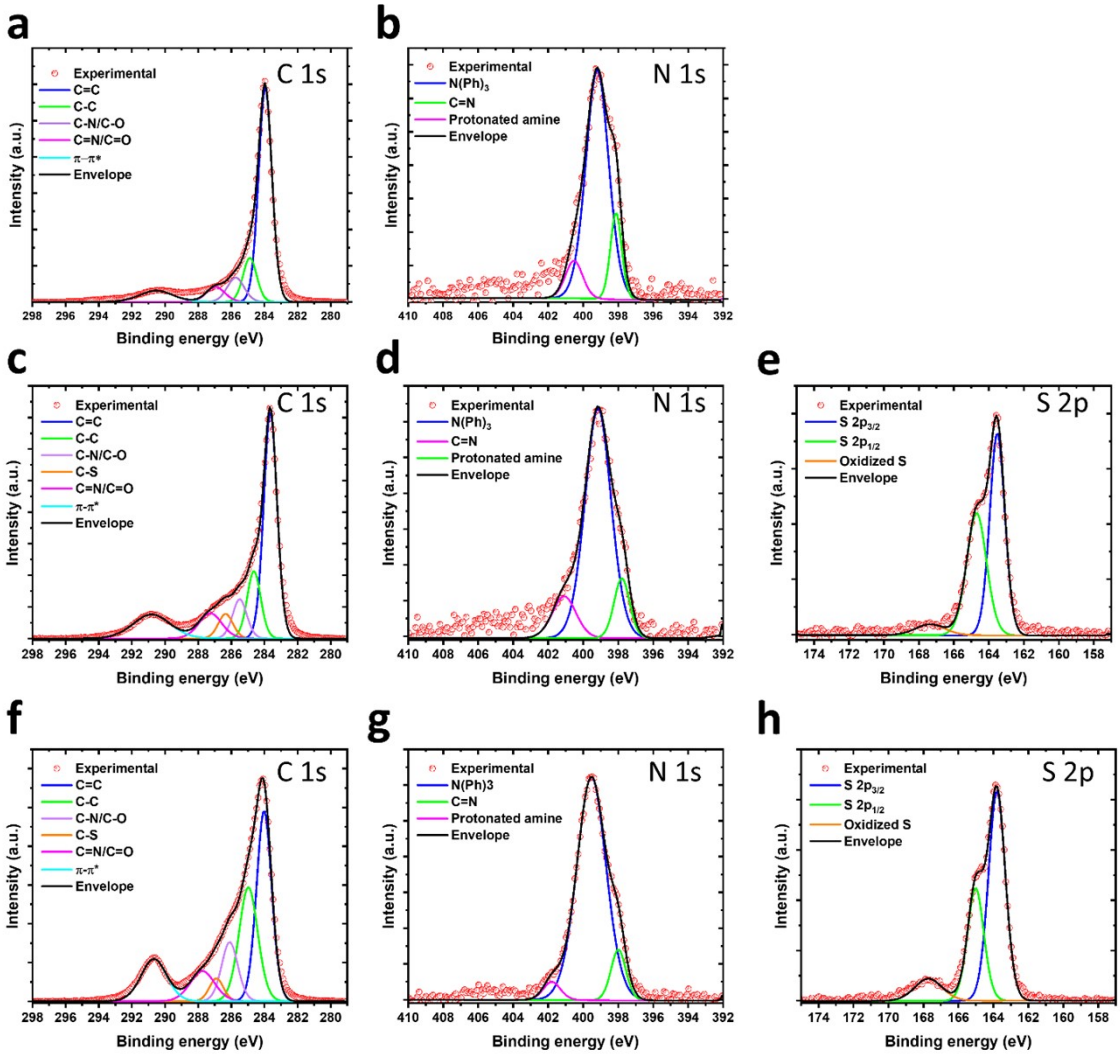

Figure S3. XPS spectra of (a, c, f) C 1s, (b, d, g) N 1s, (e, h) S 2p for (a-b) COF K60@Celgard, (c-e) KS60@Celgard and (f-h) KS80@Celgard separators.

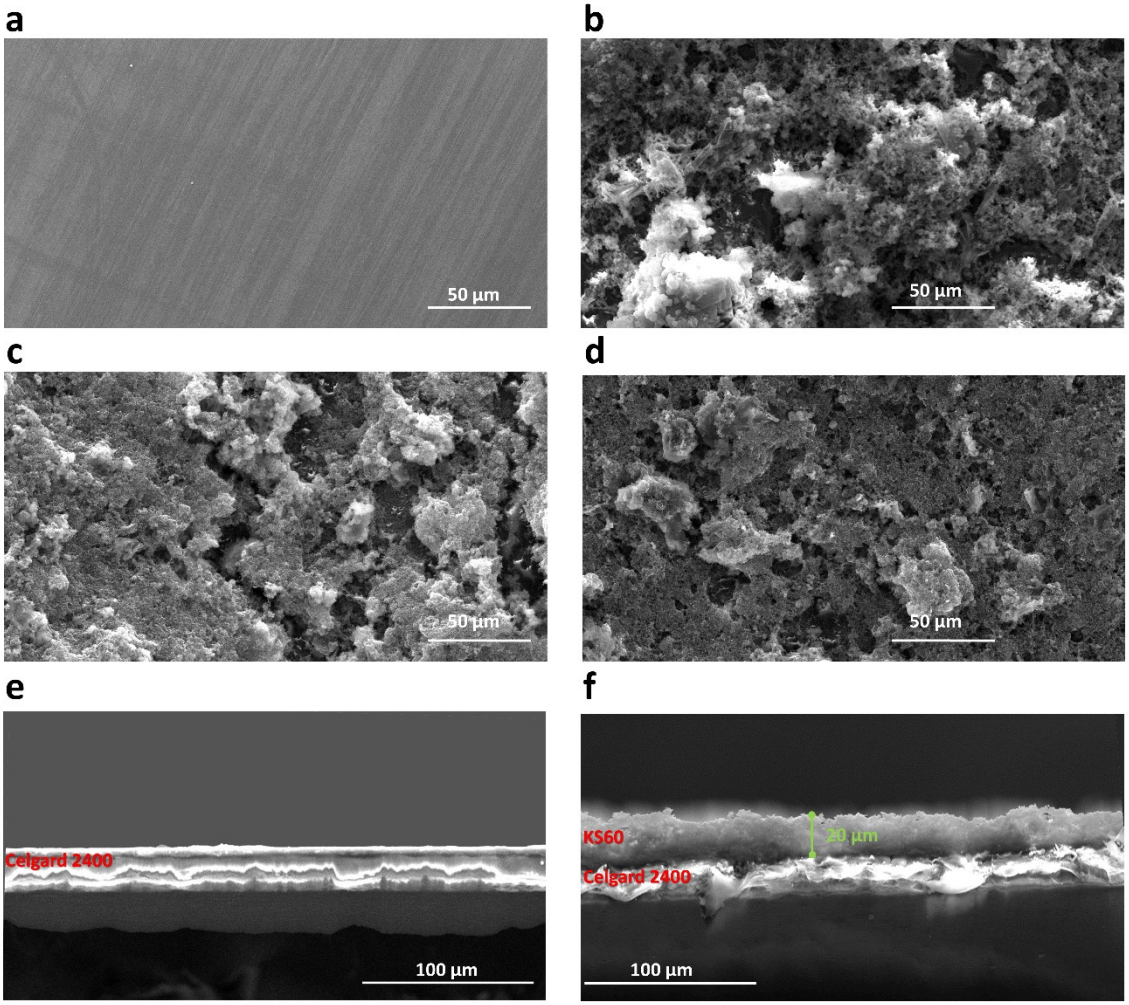

Figure S4. Low magnification SEM images of (a) Pristine Celgard, (b) KS60@Celgard, (c) K60@Celgard and (d) KS80@Celgard separators. SEM cross-sectional view of the (e) pristine Celgard 2400 and (f) KS60@Celgard separators.

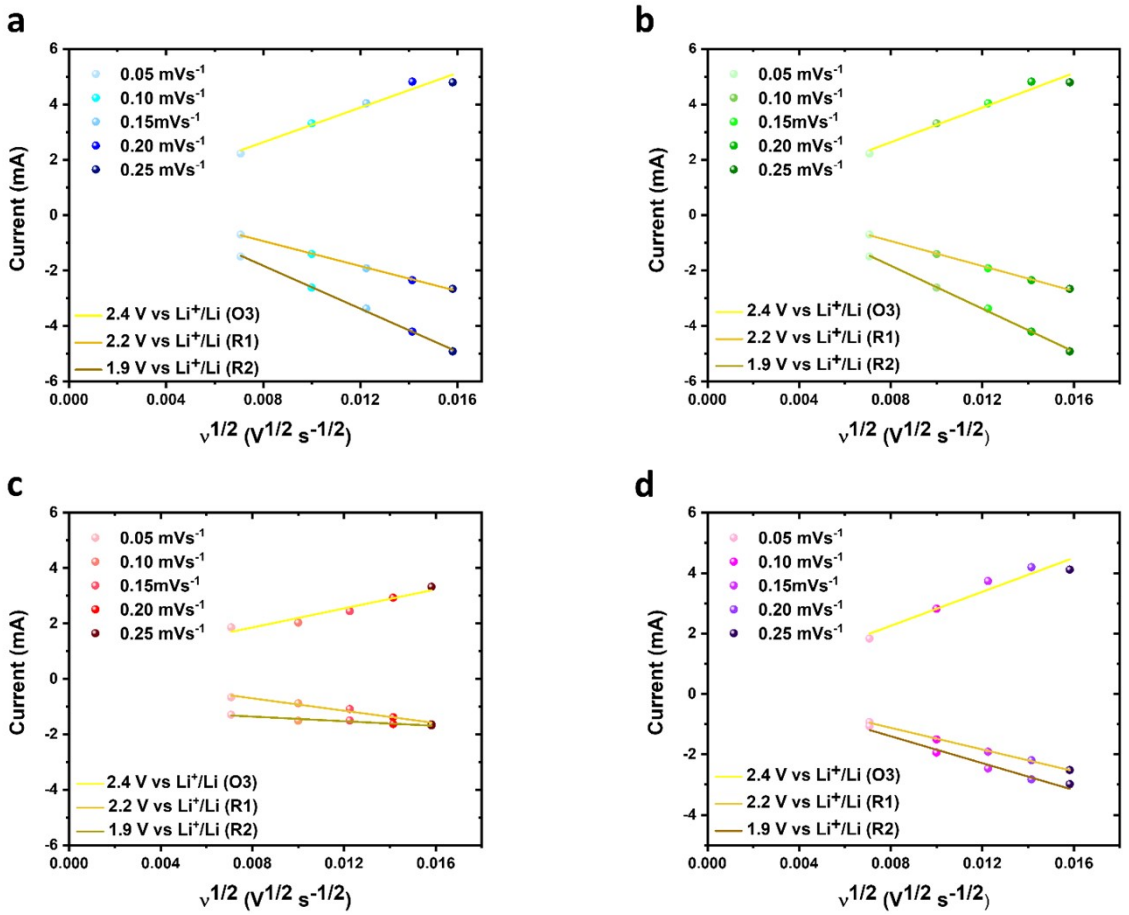

Figure S5. Linear fitting of the current vs. the square root of the potential scan rate plot, as extracted from the measurements reported in Fig. 2a-d for the LSBs based on (a) Celgard, (b) KS60@Celgard, (c) K60@Celgard and (d) KS80@Celgard separators. The slop of the linear regression is used to calculate the D_{Li^+}, using the Randles-Sevcik equation.

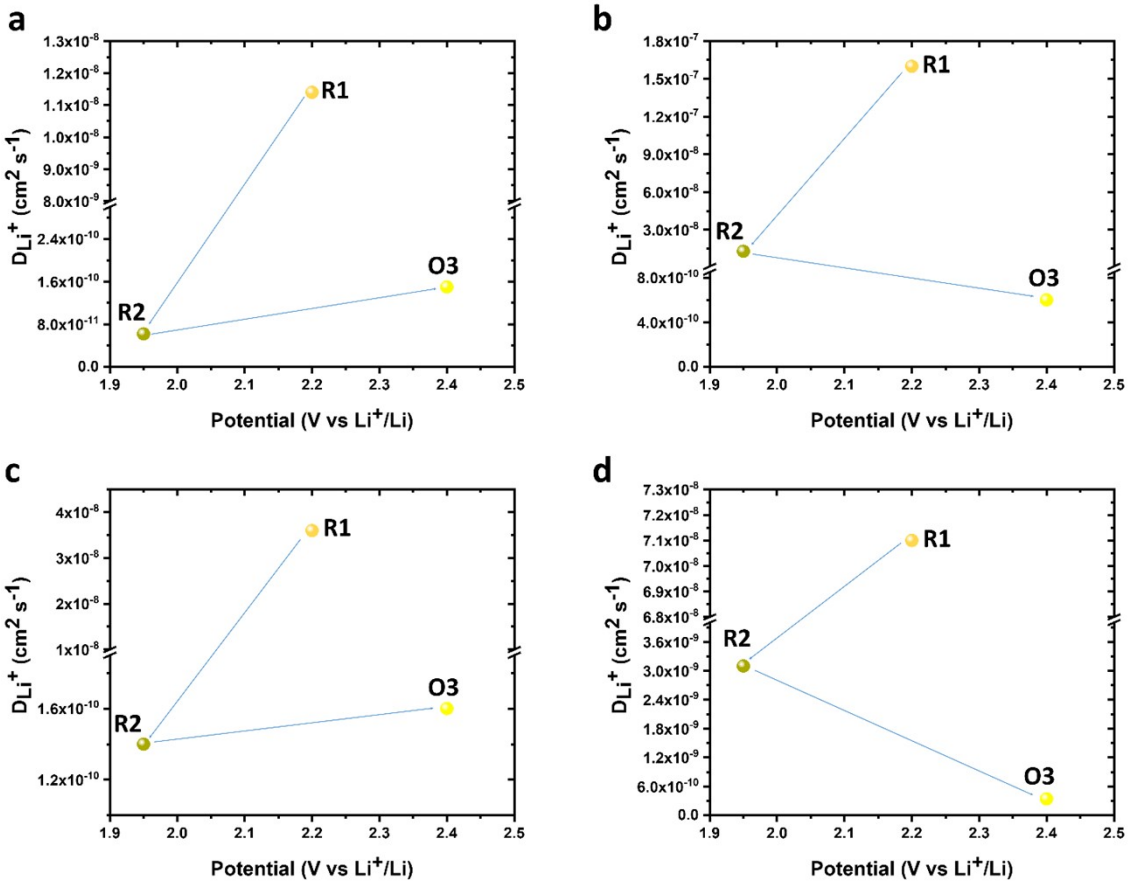

Figure S6. D_{Li}^{+} at the reduction peaks R1 and R2 at ~2.2 and ~1.9 V vs. Li^{+}/Li, respectively, and the oxidation peak O3 at 2.4 V *vs*. Li^{+}/Li, measured for the LSBs containing (a) Celgard, (b) KS60@Celgard, (c) K60@Celgard and (d) KS80@Celgard separators.

Table S2. D_{Li}^{+} calculated from the Randles-Sevcik equation by using the current values at each reduction/oxidation peak of the CV curves reported in Figure 2 and Figure S1.

Separator	Cell condition	$D_{Li}^{+}(cm^2 \cdot s^{-1})$
Celgard	Peak O3 (2.4 V)	1.5×10^{-10}
	Peak R1 (2.2 V)	1.1×10^{-8}
	Peak R2 (1.9 V)	6.2×10^{-11}
KS60@Celgard	Peak O3 (2.4 V)	6.0×10^{-10}
	Peak R1 (2.2 V)	1.6×10^{-7}
	Peak R2 (1.9 V)	1.3×10^{-8}
K60@Celgard	Peak O3 (2.4 V)	1.6×10^{-10}
	Peak R1 (2.2 V)	3.6×10^{-8}
	Peak R2 (1.9 V)	1.4×10^{-9}

KS80@Celgard	Peak O3 (2.4 V)	3.4×10^{-10}
	Peak R1 (2.2 V)	7.1×10^{-8}
	Peak R2 (1.9 V)	3.1×10^{-9}

Table S3. Equivalent circuits used to fit the the EIS spectra shown in Figure 1 and Figure S1, and R_{tot} of the cells at the OCV and after 1 and 5 CV cycles.

Separator	**Cell condition**	**Equivalent circuit**	**R_{tot} (Ω)**
Celgard	OCV	$R_e(R_1C_1)(R_2Q_2)(R_wQ_w)Q_{diff}$	41 ± 3
	After 1 CV cycle	$R_e(R_1C_1)(R_2Q_2)(R_wQ_w)Q_{diff}$	14.0 ± 0.4
	After 5 CV cycles	$R_e(R_1C_1)(R_2Q_2)(R_wQ_w)Q_{diff}$	10.6 ± 0.8
KS60@Celgard	OCV	$R_e(R_1Q_1)Q_{diff}$	56.5 ± 0.4
	After 1 CV cycle	$R_e(R_1Q_1)(R_2Q_2)(R_wQ_w)Q_{diff}$	14.2 ± 0.3
	After 5 CV cycles	$R_e(R_1Q_1)(R_2Q_2)(R_wQ_w)Q_{diff}$	6.1 ± 0.2
K60@Celgard	OCV	$R_e(R_1C_1)(R_2Q_2)(R_wQ_w)Q_{diff}$	43.4 ± 0.1
	After 1 CV cycle	$R_e(R_1C_1)(R_2Q_2)(R_wQ_w)Q_{diff}$	7.7 ± 0.1
	After 5 CV cycles	$R_e(R_1C_1)(R_2Q_2)(R_wQ_w)Q_{diff}$	6.2 ± 0.2
KS80@Celgard	OCV	$R_e(R_1C_1)(R_2Q_2)(R_wC_w)Q_{diff}$	43 ± 1
	After 1 CV cycle	$R_e(R_1C_1)(R_2Q_2)(R_wC_w)Q_{diff}$	25± 3
	After 5 CV cycles	$R_e(R_1C_1)(R_2Q_2)(R_wQ_w)Q_{diff}$	16 ± 1

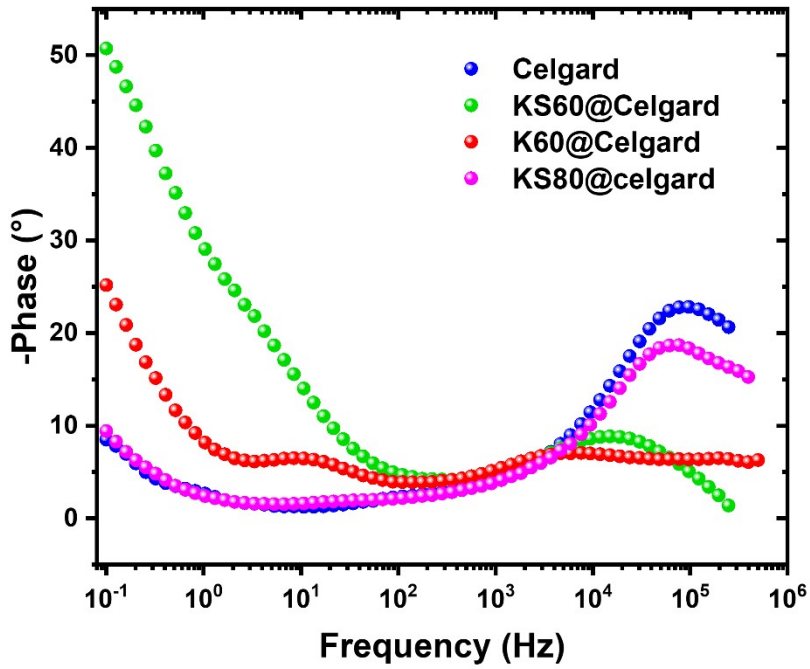

Figure S7. Phase angle Bode plots measured in the 500 kHz-100 mHz frequency range for all the investigated LSBs.

Table S3. Specific discharge capacity measured at different C-rates for the LSBs based on pristine Celgard, KS60@Celgard K60@Celgard and KS80@Celgard separators.

	Specific discharge capacity (mA h s^{-1})						
Current rate / Sepa-rator	C10	C8	C5	C3	C2	1C	C10
Celgard	825	704	643	607	579	504	681
KS60@Celgard	1017	933	864	791	709	651	951
K60@Celgard	1071	1028	262	200	152	44	1068
KS80@Celgard	843	733	684	641	559	150	712

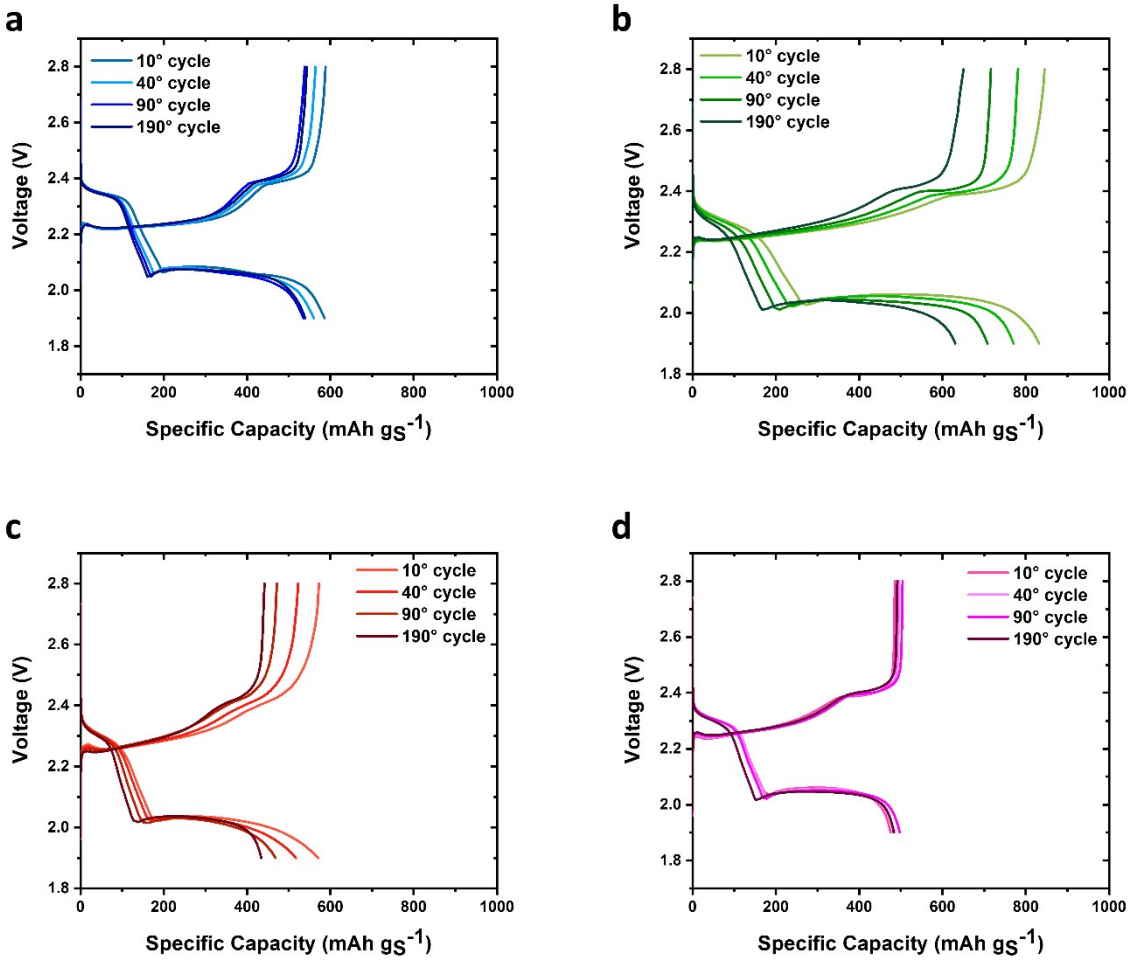

Figure S8. Selected GCD profiles measured at C5 rate for the LSBs (sulfur loading: ~2 mg cm^{-2}; E/S ratio: 15 µL mg_S^{-1}, electrode geometric area: 1.54 cm^2) based on (a) pristine Celgard, (b) KS60@Celgard, (c) K60@Celgard and (d) KS80@Celgard separators.

Table S5. Comparison between the performances of different LSBs based on COF-based functional separators reported in literature.

Separator	Sulphur loading (mg cm^{-2})	Specific Discharge capacity (mA h g^{-1})	C-rate	Capacity retention (%)	Reference
TpPa-SO_3Li@Celgard	1.5	939.4	C5	55.1, after 100 cycles	[1]
TpPa-$(SO_3)_2$@Celgard	1.3-1.5	1036	C5	82.5, after 100 cycles	[2]
TpPa-SO_3H@PP	1	1000	C5	92.5, after 100 cycles	[3]
TP-BDP@Celgard	1-1.5	1247	C5	50, after 100 cycles	[4]
TpPa-$(SO_3)_2$@Celgard	1.2-2.0	890	C2	70.9, after 200 cycles	[5]
Py-BBT@Celgard	1	1249	C2	72.5, after 100 cycles	[6]
BTFMB-	1	1205	C5	83.2, after	[7]

TzDa@Celgard				100 cycles	
KS60@Celgard	2.4	850	C5	74.1, after 190 cycles	This work

Tp: triformylphloroglucinol; **Pa-SO_3**: 2,5-diaminobenzenesulfonic acid; **Pa-$(SO_3)_2$**: 2,5-diaminobenzene-1,4-disulfonic acid
PP: polypropylene
TP: 2,4,6-trihydroxybenzene-1,3,5-tricarbaldehyde; **BPD**: benzidine dihydrochloride
Py: 4,4',4'',4'''-(pyrene-1,3,6,8-tetrayl)tetraaniline; **BBT**: benzobisthiadiazole-containing diamine
BTFMB: 3,5-bis(trifluoromethyl)benzyl; **Tz**: 4,4',4''-(1,3,5-triazine-2,4,6-triyil)trianiline; **Da**: 2,5-dihydroxyterephthalaldehyde

Table S6. Band assignment and the atomic percentage of the corresponding sulfur species for the ex-situ high-resolution XPS S 2p spectra of pristine Celgard, KS60@Celgard K60@Celgard and KS80@Celgard separators, obtained by disassembling the investigated LSBs in charged state after 190 GCD cycles.

Separator	Band assignment	Binding energy (eV)	Atomic percentage of S species associated to the assigned band (%)
Celgard	S_8	164.19 (165.29)	10.15 (6.05)
	Bridged S-S	162.13 (163.43)	8.04 (3.64)
	Terminal S-Li	161.41 (162.80)	41.47 (28.71)
	Li_2S	159.40 (160.05)	1.27 (0.67)
KS60@Celgard	S_8	165.39 (166.41)	20.31 (11.21)
	Bridged S-S	163.83 (164.86)	12.35 (5.35)
	Terminal S-Li	161.80 (162.72)	29.49 (15.10)
	Li_2S	159.48 (160.20)	1.70 (4.49)
K60@Celgard	S_8	165.08 (166.04)	12.50 (6.42)
	Bridged S-S	163.41 (164.15)	22.18 (14.31)
	Terminal S-Li	161.64 (162.61)	27.70 (12.27)
	Li_2S	159.83 (160.51)	3.05 (1.57)
KS80@Celgard	S_8	165.27 (166.06)	12.16 (7.18)
	Bridged S-S	163.70 (164.79)	13.71 (7.77)
	Terminal S-Li	161.57 (162.48)	33.00 (23.27)
	Li_2S	159.64 (160.61)	1.91 (1.00)

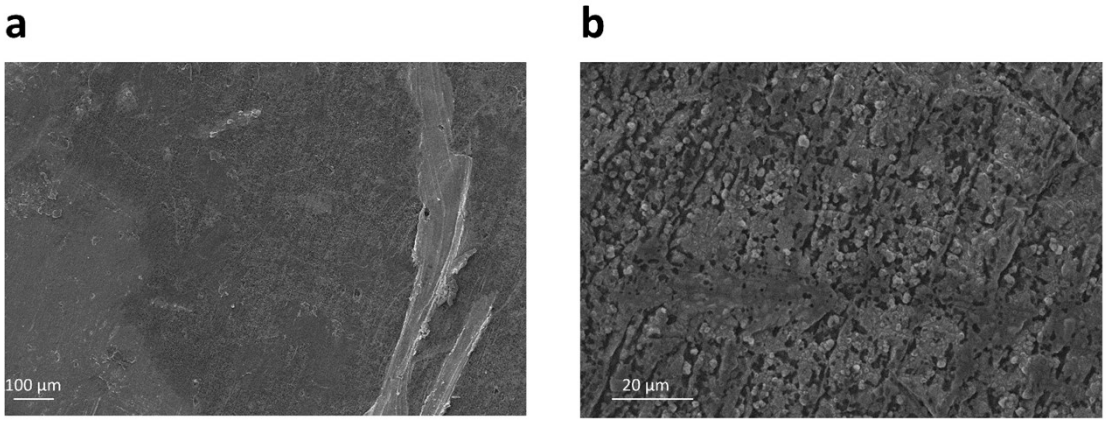

Figure S9. (a) Low- and (b) high-magnification SEM images of a fresh Li anode.

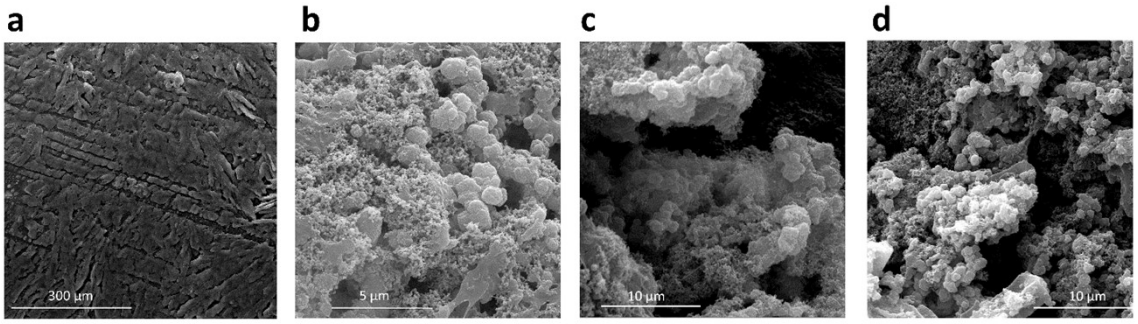

Figure S10. SEM images of the (a) Celgard, (b) KS60@Celgard, (c) K60@Celgard and (d) KS80@Celgard separators obtained by disassembling the investigated LSBs in charged state after 190 GCD cycles.

Supporting Note 1

Computational results. As a preliminary step towards the study of the adsorption energy of Li_2S_x on K1 and KS1 COFs, we performed density functional theory (DFT) simulations starting from a 1x1x2 supercell of the crystal structures already reported in literature [8-10](Figure S11-S12; see below for methods). We observed that, by nudging one of the two COF layers in the cell, the geometry optimization yields the structures reported in Fig. S11-S12. The energy of the obtained structures, with a different stacking geometry, is lower compared to the reported structures by 5.1 and 0.9 eV per unit cell for K1 and KS1, respectively. As these energy differences are significantly greater than the typical DFT accuracy, we conclude that the reported eclipsed structures, may not be the most energetically favored for the studied COFs. However, it is worth to note that the structures we obtained from DFT geometry optimization may not be the lowest-energy structures for the two COFs, as a consequence of the structural complexity of the studied system. The structures reported in Figure S11-S12 are the closest local minimum, that is lower in energy than the previously reported eclipsed structures. Thus, the calculated energy differences represent a lower bound to the actual difference between the eclipsed and the minimum-energy structure. More energetically favourable stackings may also exist, thus making the eclipsed structure even more unstable.

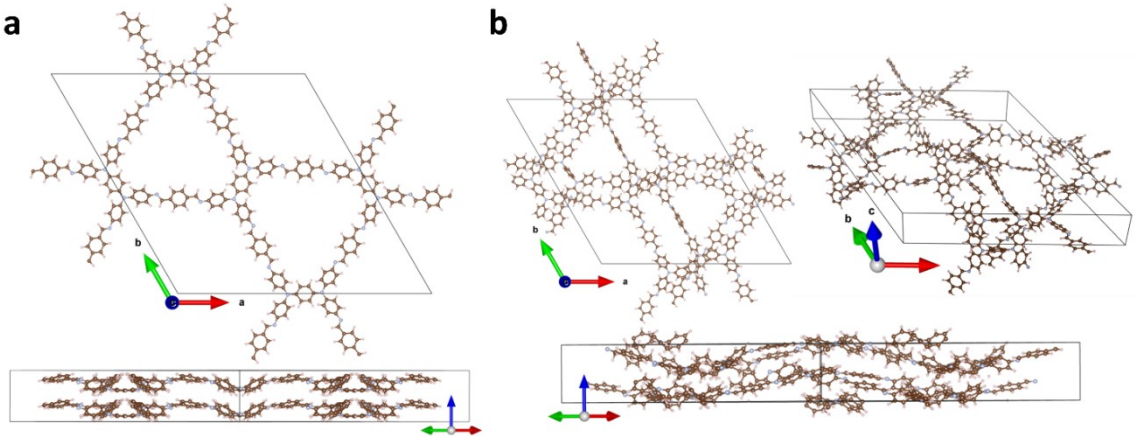

Figure S11. Crystal structures of K1 COF: (a) reported structure and (b) lower-energy structure obtained from DFT geometry optimization, shown in different orientations. C, H, and N atoms are represented as brown, white, and blue spheres, respectively. Solid, black lines represent the crystallographic cell.

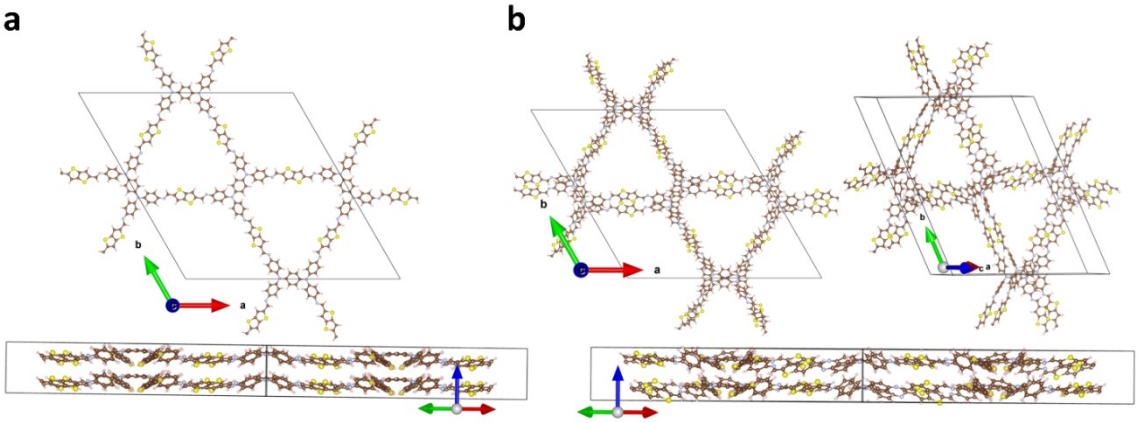

Figure S12. Crystal structure of KS1 COF: (a) reported structure and (b) lower-energy structure obtained from DFT geometry optimization, shown in different orientations. C, H, S and N atoms are represented as brown, white, yellow, and blue spheres, respectively. Solid, black lines represent the crystallographic cell.

Finally, we note that the stacking geometry does not have a strong influence on the X-ray diffraction (XRD) pattern, especially for low-angle reflections, as shown in Figure S13. This is particularly evident in KS1, whose final geometry differs from the reported crystal structure by the stacking type, while in K1 the COF geometry itself rearranges during geometry optimization. The structural complexity would require a more accurate interpretation of the experimental PXRD patterns and those of the simulated structures to determine reliably the stacking geometry of these COFs. Indeed, the stacking of the 2D sheets to form a layered eclipsed or staggered structure with highly ordered pore channels, can play a major role in the charge migration and ionic transport through the framework when a COF layer is used as separator coating, influencing the Li2Sx shuttle and the redox kinetics.[11, 12] However, this study goes beyond the scope of this work.

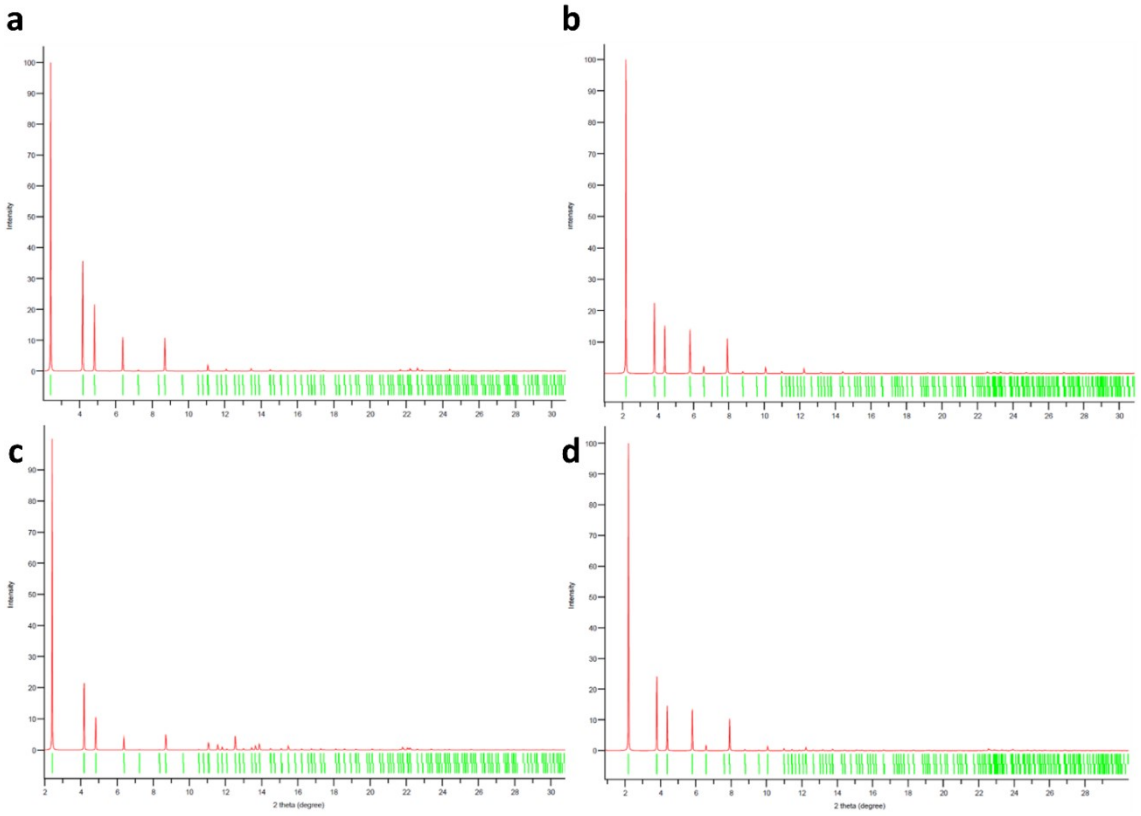

Figure S13. Simulated XRD patterns of (a, b) K1 and (c, d) KS1 COFs. (a, c) XRD pattern of the eclipsed crystal structures as reported in literature. (b, d) XRD pattern of the structures obtained in this work from DFT geometry optimization.

Construction of the initial structures. The initial structure of K1 was constructed on the base of the data reported in reference[8], while reference[10] reports the unit cell of KS1 without providing the atomic positions. Since KS1 differs from K1 only by one functional group in the linker (thienothiophene *vs.* phenyl), we built the KS1 crystal structure by adopting the KS1 unit cell, the K1 atomic positions, and substituting the linking phenyl with thienothiophene rings, and optimizing the atomic positions through DFT.

Methods for density function theory simulations. DFT simulations were run through the VASP code[13] within the plane augmented wave framework.[14] The PBE functional[15] was adopted throughout. The plane wave energy cutoff was set to 400 eV. Given the large cells adopted in the simulations (504 atoms for both K1 and KS1), which entail large computational requirements, we performed the simulations by sampling the reciprocal space through one k point (Gamma-only). The geometry optimization and self-consistent field procedures were stopped when the energy difference between two consecutive steps was lower than 10^{-4} and 10^{-5} eV, respectively. Only atomic positions inside the unit cells were optimized, whereas the unit cell parameters were kept frozen at those determined experimentally in references [8] and [10]. Structures drawings and simulated XRD patterns were obtained through the VESTA code.[16]

REFERENCES

1. C. Li, A. L. Ward, S. E. Doris, T. A. Pascal, D. Prendergast and B. A. Helms, *Nano Letters*, 2015, **15**, 5724-5729.
2. J. Xu, S. An, X. Song, Y. Cao, N. Wang, X. Qiu, Y. Zhang, J. Chen, X. Duan, J. Huang, W. Li and Y. Wang, *Advanced Materials*, 2021, **33**, 2105178.
3. J. Zhao, G. Yan, X. Zhang, Y. Feng, N. Li, J. Shi and X. Qu, *Chemical Engineering Journal*, 2022, **442**, 136352.
4. Q. Xu, K. Zhang, J. Qian, Y. Guo, X. Song, H. Pan, D. Wang and X. Li, *ACS Applied Energy Materials*, 2019, **2**, 5793-5798.

5. T. Xia, Z. Wu, Y. Liang, W. Wang, Y. Li, X. Tian, L. Feng, Z. Sui and Q. Chen, *Journal of Colloid and Interface Science*, 2023, **645**, 146-153.
6. R. Wang, Q. Cai, Y. Zhu, Z. Mi, W. Weng, Y. Liu, J. Wan, J. Hu, C. Wang, D. Yang and J. Guo, *Chemistry of Materials*, 2021, **33**, 3566-3574.
7. S. Pang, Y. Liu, Z. Zhang, Y. Li, C. Li, Z. Shi and S. Feng, *New Journal of Chemistry*, 2024, **48**, 16-20.
8. Q. Hao, Z.-J. Li, B. Bai, X. Zhang, Y.-W. Zhong, L.-J. Wan and D. Wang, *Angewandte Chemie International Edition*, 2021, **60**, 12498-12503.
9. M. Wu, Y. Zhao, R. Zhao, J. Zhu, J. Liu, Y. Zhang, C. Li, Y. Ma, H. Zhang and Y. Chen, *Advanced Functional Materials*, 2022, **32**, 2107703.
10. L. He, B. Li, Z. Ma, L. Chen, S. Gong, M. Zhang, Y. Bai, Q. Guo, F. Wu, F. Zhao, J. Li, D. Zhang, D. Sheng, X. Dai, L. Chen, J. Shu, Z. Chai and S. Wang, *Science China Chemistry*, 2023, **66**, 783-790.
11. Z. Cheng, H. Pan, H. Zhong, Z. Xiao, X. Li and R. Wang, *Advanced Functional Materials*, 2018, **28**, 1707597.
12. J. Wang, L. Si, Q. Wei, X. Hong, S. Cai and Y. Cai, *ACS Applied Nano Materials*, 2018, **1**, 132-138.
13. G. Kresse and J. Furthmüller, *Computational Materials Science*, 1996, **6**, 15-50.
14. P. E. Blöchl, *Physical Review B*, 1994, **50**, 17953-17979.
15. J. P. Perdew, K. Burke and M. Ernzerhof, *Physical Review Letters*, 1996, **77**, 3865-3868.
16. K. Momma and F. Izumi, *Journal of Applied Crystallography*, 2011, **44**, 1272-1276.